

# Molecular Dynamics Simulation of The Force-extension Relation in Simple Models of Semiflexible Biopolymers

by

Scott Cheng Hsin Yang

A THESIS SUBMITTED IN PARTIAL FULFILMENT OF  
THE REQUIREMENTS FOR THE DEGREE OF

Bachelor of Science

in

Faculty of Science

(Physics)

The University Of British Columbia

April, 2006

© Scott Cheng Hsin Yang 2006

# Abstract

The elasticity of flexible and semi-flexible bio-polymers are studied by means of molecular dynamics simulation. The bio-polymers are represented by coarse-grained model with the Lennard-Jones potential, the finitely-extensible non-linear elastic potential, and the angle-bending potentials. The main goal is to verify the analytic results of entropic elasticity for the semiflexible case through the implementing of the coarse-grained model. The simulation data shows agreement with the analytical model in its scaling properties and the distribution of end-to-end distance. The rich results show a spectrum of elasticities ranging from flexible, semiflexible, to rigid-rod like. The flexible and semiflexible simulation data are in excellent agreement with the theoretical predictions. Time scale of force convergence and force-extension reliability under tension are also explored. The study can be further extended to the force-extension relation of dilute cross-linked bio-polymers.

Scott Cheng Hsin Yang. chsy@physics.ubc.ca

# Table of Contents

<b>Abstract</b>	ii
<b>Table of Contents</b>	iii
<b>List of Tables</b>	v
<b>List of Figures</b>	vi
<b>Acknowledgements</b>	viii
<b>1 Introduction</b>	1
<b>2 Theory</b>	5
2.1 Properties of Polymer Chains: Random Walk	5
2.2 The Origin of Polymer Elasticity	8
2.2.1 The Force-Extension Relation of The FJC Model	9
2.2.2 The Force-Extension Relation of The WLC Model	12

*Table of Contents*

---

<b>3</b>	<b>Methodology: Molecular Dynamics Simulation</b>	<b>15</b>
3.1	The Bead-stick Model	16
3.2	Numerical Integrator	21
3.3	Force-extension Measurement	25
<b>4</b>	<b>Results</b>	<b>28</b>
4.1	Properties of Random-Walking Chain	29
4.2	The Entropic Spring Constant	31
4.3	Elasticity Spectrum	38
4.3.1	From Flexible to Semiflexible	40
4.3.2	Angle Potential and Persistence Length	43
4.3.3	Transition to Semi-rigid Rod	45
4.4	Force Convergence	48
<b>5</b>	<b>Conclusion</b>	<b>52</b>
5.1	Outlook	54
	<b>Bibliography</b>	<b>56</b>

# List of Tables

2.1	Frequently used symbols and abbreviations . . . . .	14
3.1	Reduced LJ units . . . . .	18
4.1	Fitted values of $\ell_p$ . . . . .	45

# List of Figures

1.1	Pulling experiment. . . . .	2
3.1	Configuration of the bead-stick model . . . . .	17
3.2	The LJ and the FENE potentials. . . . .	20
3.3	Flowchart of the MD simulation . . . . .	24
3.4	Force measurement set up . . . . .	26
4.1	R-N relation . . . . .	30
4.2	Distribution of the end-to-end distance. . . . .	32
4.3	Flexible force-extension data and gaussian FJC prediction. . .	33
4.4	Force-extension relations with varying T and N . . . . .	35
4.5	Temperature dependence of the entropic spring constant. . .	36
4.6	N dependence of the entropic spring constant. . . . .	37
4.7	Normalization of the F-R relation. . . . .	39

## *List of Figures*

---

4.8	Flexible and semiflexible F-R relations fitted with the theoretical models . . . . .	41
4.9	Fitting WLC solution to semiflexible F-R relation for $K_A$ 2 and 3. . . . .	44
4.10	F-R relation of high values of $K_A$ . . . . .	47
4.11	F-R relation under tension. . . . .	50
4.12	Time scale of force convergence. . . . .	51

# Acknowledgements

Incredibly many thanks to my supervisor Professor Rottler.



# Chapter 1

## Introduction

About fifteen years ago, technology has advanced to that a single biopolymer manipulation became possible. One of the first pulling experiment of single molecules of DNA was done by Smith et al. in 1992 [1]. The delicate force-extension experiment triggered a rapidly increasing interest among the experimentalists and the theorists to better understand the mechanical properties of biopolymers. On the experimental side, experimentalists are still striving to find methods that can cover a larger range of force-extension with more precision. Fig. 1.1 shows schematically how pulling experiments are done. The newest technology is to use optical traps such as laser trap to pull on molecules. The biopolymer chain is fixed at one end on a pipette and attached to the trapped molecule at the other end. Through the optical trap method, precise forces can be applied to the biopolymer chain, and its extension can be measured to produce the force-extension relations. Older experimental techniques include magnetic pulling and fluid flow all work the same way.

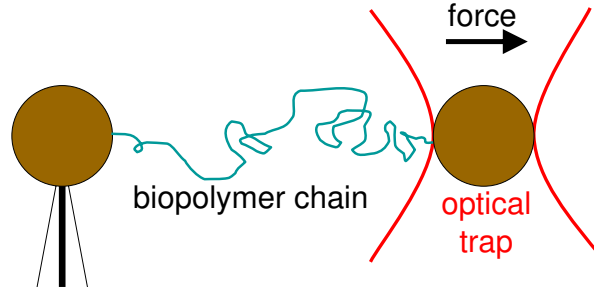


Figure 1.1: This is a schematic representation of a pulling experiment. The single biopolymer, usually DNA, is fixed at one end to the pipette and pulled on the other end using a molecular optical trap [2].

On the side of theory, the theory of fully flexible polymer elasticity are well tested and understood by virtues of the freely-jointed chain (FJC) model. The new experiment on revealing biopolymer elasticity of course attracts the theorists as well. Even up until today, theorists continue to propose models to describe the DNA experimental data. About a decade ago, Marko and Siggia [3] treated the worm-like chain (WLC) model numerically and obtained a solution that describes the data from Smith et al.'s DNA pulling experiment very well. This became one of the theoretical basis in biopolymer elasticity. Recently, researchers became interested in the mechanical properties of cross-linked semiflexible biopolymer networks like actin. The experiment done by Gardel et al. on stretching cross-linked and bundled F-actin has shown that the elasticity of cross-linked systems is sensitive to cross-link concentration and has two distinct regimes of force-

extension behavior [4]. This is the frontier of polymer physics that is still poorly understood. For complicated systems like a network, MD simulations are useful for testing theoretical models that may provide insights and explanation of the mechanical behavior of network elasticity.

This project, in the context mentioned above, aims for the understanding of the force-extension relation in single semi-flexible bio-polymers such as DNA using coarse-grained models through molecular dynamics (MD) simulations. The goal is to see whether certain entropic contributions to the elasticity of stiff polymers can be sampled in molecular dynamics. At sufficiently short time scales, this will provide important building blocks towards a larger study of the mechanical properties of semi-flexible bio-polymers networks. The scope of the project covers two of the simplest models, namely the FJC and the WLC model. The MD simulation data are compared with the well-established theoretical models for an indication of the power of MD simulation in reproducing experimental results and test theory.

The knowledge of the force-extension relation of bio-polymers helps to explain many biological phenomena such as rigidity of cell walls. The most popular topic in this field is probably the understanding of the molecular-scale interaction between protein and DNA in the replication process [2]. It also contributes to mechanical research of structure and mechanical strength

of DNA, actins, and many other biopolymers. Polymer synthesis and bio-engineering would also benefit from such knowledge. The hope of building bio-machines and bio-molecular motors with nanotechnology heavily depends on the understanding of biopolymer elasticity. As in the first Advance Nanotechnology Conference held in 2004, Tucker, Vogel, and Hess [5] proposed a molecular shuttle system that is able to shuttle molecular-sized objects. The moving track is built with biopolymer antenna. The understanding of force-extension relation would help to ensure smooth shuttling process. In conclusion, the importance of the understanding of bio-polymer elasticity is broadly acknowledged.

Following the introduction, there will be a theory section which briefly points out the physics behind the two theoretical models used. A chapter on Methodology, which is the MD simulation, will then be given in particular to describe the simulation model used and the basics of MD integrator. From there, a Results chapter with discussion will be presented. Finally, there is a Conclusion chapter to summarize and conclude the work done and layout general directions for future work.

# Chapter 2

## Theory

When biopolymers are placed in solutions, the solvent particles collides with the biopolymers randomly, resulting in a kind of elasticity. This effect can be seen as a performance of a three dimensional random walk by the biopolymers. This chapter is split into two sections. The first introduces a gaussian approximation of the conformational distribution of a random walker via the freely-jointed chain (FJC) model. The second section connects the pulling force with the distribution using statistical mechanics and presents the force-extension (F-R) relation of the flexible FJC model and of the semiflexible worm-like chain (WLC) model. Crucial differences between the two theoretical models are discussed.

### 2.1 Properties of Polymer Chains: Random Walk

To begin, the FJC model is composed of  $N$  equal-length rigid rods joined together by point monomers. The monomers impose no bending or rotation

constraint. The end-to-end vector is then

$$\vec{R} = \sum_{i=1}^N \vec{b}_i, \quad (2.1)$$

where  $b_i$  represents the vector of the  $i^{th}$  rod. Inside a solution, an unstressed FJC performs an ideal 3-D random walk. An important property of such a chain is its scaling, namely the relationship between the end-to-end distance,  $R$ , and  $N$ . This can be found by considering the dot product of Eq. (2.1) with itself:

$$\langle R^2 \rangle = \left\langle \sum_{i=1}^N \sum_{j=1}^N \vec{b}_i \cdot \vec{b}_j \right\rangle = \sum_{i=1}^N \sum_{j=1}^N \langle \vec{b}_i \cdot \vec{b}_j \rangle = \sum_{i=1}^N \langle \vec{b}_i \cdot \vec{b}_i \rangle + \sum_{i \neq j}^N \langle \vec{b}_i \cdot \vec{b}_j \rangle.$$

The second term in the last equality sums up to zero because each rod is isotropic and uncorrelated in a random walk. The final result is then

$$\langle R^2 \rangle = b^2 N \quad (2.2)$$

For a more realistic model, one replaces the point monomers with hard spheres to prevent the chain from crossing itself. This introduces a volume exclusion effect into the model. The movement of this chain in solution is called a self-avoiding walk (SAW). With the effect of the excluded volume,

the R-N relation becomes

$$\langle R^2 \rangle \propto N^{6/5}, \quad (2.3)$$

where the exponent 6/5 is the Flory exponent in 3-dimensions [6]. Comparing the exponent in the above equation with the one in Eq. (2.2), one notices the increase in exponent, which is expected for non-ideal random walks. With exclusion volume, there is a non-zero minimum separation between each segments, forcing the segments to spread out. The chain inevitably spreads out. The result is then an increase in the exponent.

Another important property of random walkers is that with  $N \gg 1$  and a large sampling of chain configurations, the distribution of  $\vec{R}$  approaches a gaussian distribution as stated in the central limit theorem. For a 3-D random walk, the resulting probability distribution of  $\vec{R}$  one obtains is the 3-D gaussian

$$P(\vec{R}) = P(x)P(y)P(z) = \left( \frac{3}{2\pi b^2 N} \right)^{3/2} \exp \left[ \frac{-3R^2}{2 b^2 N} \right], \quad (2.4)$$

where  $R^2$  is really the vector equation in Eq. (2.2) [7]. It shows that the coordinates of both ends of the chain is most likely to be at (0, 0, 0), and should not be confused with the distribution of the end-to-end distance R

[8] which is

$$P(R) = 4\pi R^2 P(\vec{R}). \quad (2.5)$$

The factor of  $4\pi R^2$  accounts for the fact that there are more coordinates on a sphere if the radius is larger.

## 2.2 The Origin of Polymer Elasticity

The origin of elasticity is entropy. From Eq. (2.4), we know that a polymer in solution has a distribution of  $\vec{R}$  that is centered at zero. Statistical mechanics links the distribution of  $\vec{R}$  to entropy [7]:

$$S(R) = k_B \ln P(\vec{R}) = \frac{-3R^2}{2b^2 N} + \text{constant}, \quad (2.6)$$

where  $k_B$  is the boltzmann constant. The above equation is at its maximum when  $R=0$ . This means that a polymer has access to the most number of configurations when the extension  $R$  equals zero. Physically, one can imagine fixing a polymer's end-to-end distance with pins. At small extensions, a polymer has access to so many configurations that it would rarely come to a conformation that pulls on the pins. On the contrary, at large extensions, the chain would almost always come to such pulling configurations. From the point of view of entropy, the chain loses entropy as it is extended from



small  $R$  to large  $R$ . The pulling force then emerges from paying an entropy penalty.

### 2.2.1 The Force-Extension Relation of The FJC Model

Statistical mechanics further tells us that force is related to the free energy, which has the form

$$F(R) = U - TS(R), \quad (2.7)$$

where  $T$  is the temperature and  $S(R)$  is the entropy from Eq. (2.6). Here, the internal energy does not contribute to the free energy because the internal structure of a FJC will not change in the process of pulling. Taking the derivative of the free energy, one obtains the purely entropic F-R relation [7]:

$$\frac{\partial F(R)}{\partial R} = f(R) = \frac{3k_B T}{b^2 N} R. \quad (2.8)$$

The main feature of this formula is that the force is linearly proportional to  $R$  like a Hookeian spring. This simple result is a good approximation for small extensions, where small  $R$  means  $R$  less than half of the total contour length,  $L$ . As  $R$  approaches  $L$ , one expects the force to diverge because it requires an infinitely large force to extend the length of a rigid rod. Close to that limit, the gaussian approximation to  $P(\vec{R})$  apparently fails to give

the correct entropy contribution.

Though only an approximation, Eq. (2.8) gives some insights to the physics of polymer elasticity. One may identify the prefactor in Eq. (2.8) as a spring constant. This entropic spring constant has the following dependence:

$$k_{entropy} \propto T \propto \frac{1}{N}. \quad (2.9)$$

The dependence on  $T$  is a signature of entropic springs. Physically, as temperature increases, the increasing random kicking from solution provides energy to the polymers to explore the accessible configurations more rapidly. The result is that the polymers are more likely to be in the pulling conformations. The temperature dependence of F-R relation is a general property of all polymers, including semiflexible and cross-linked biopolymers. The second dependence on  $1/N$  shows that as  $N$  increases, the linear elastic region increases since  $L=Nb$ . It can also act as a limiting criterion on  $N$  as to the smallest  $N$  that would still allow the FJC model to be a good approximation of real polymers. This would save time and computation power in simulations.

While  $k_{entropy}$  explains the elasticity of flexible polymers in the small extensions regime well, the more interesting part is the non-linear elasticity

at large extensions. At large extensions, the chain is no longer a random walker. Each rod is rather anisotropic, restricted to the direction of the applied force. This is the same effect as dipole moments in a magnetic field. The full treatment is done by Kuhn and Grun using Langevin chain statistics, which accounts for the fact that under large tension, all rods would line up and the chain cannot be extended more [9]. The result they obtained is

$$\frac{R}{L} = \coth\left(\frac{2\ell_k f}{k_B T}\right) - \frac{k_B T}{2\ell_k f}, \quad (2.10)$$

where  $\ell_k$  is called the Kuhn length and is equal to  $b/2$  [8]. The right hand side of the equation is in the form of the Langevin function. This equation provides the right asymptotic results that as  $R \rightarrow L$ , the corresponding  $f \rightarrow \infty$  and as  $R \rightarrow 0$ , the corresponding  $f \rightarrow 0$ . To determine the F-R relation close to full extension, the first Pade approximant of the inverse Langevin function is useful [10]. Applying the inverse Langevin function to both sides of Eq. (2.10), the F-R relation then is

$$\frac{2\ell_k f}{k_B T} \approx (R/L) \frac{3 - (R/L)^2}{1 - (R/L)^2}. \quad (2.11)$$

For small extensions, one finds that the above equation converges to Eq. (2.8). However, as  $R/L \rightarrow 1$ , one can show that  $f(R) \propto 1/[1 - (R/L)^2]$ .

This is distinctly different from the gaussian approximation of  $f(R) \propto R$ .

### 2.2.2 The Force-Extension Relation of The WLC Model

The FJC model is not really physical in having discrete segments and being totally flexible at the point monomers. A more realistic model is a continuous flexible thread model called the worm-like chain (WLC) model. There are a few ways to look at the differences between the two models. From the point of view of a FJC, a WLC is only semiflexible in that it does not bend into sharp corners but bend into arcs. This would correspond to a bending limitation in the flexible FJC model. From the perspective of a WLC at large extension, an FJC lacks the excited transverse modes of rod-bending which in reality would contribute to the free energy. In fact, the effective energy for a stretched WLC,

$$\frac{E}{k_B T} = \int_0^L ds \left( \frac{\ell_p}{2} \left| \frac{d\vec{t}}{ds} \right|^2 - f \vec{R} \right), \quad (2.12)$$

depends on  $d\vec{t}/ds$ , which is the curvature of the chain [3]. The curvature square dependence of the effective energy is a signature of the energy of a slightly bent rod [11].

The exact solution of the F-R relation for the WLC model was numerically solved by Marko and Siggia [3]. They also derived an analytical

interpolation formula

$$f(R/L) = \frac{k_B T}{\ell_p} \left( \frac{R}{L} + \frac{1}{4(1 - R/L)^2} - \frac{1}{4} \right), \quad (2.13)$$

where  $\ell_p$  is called the persistence length, describing the characteristic length over which the tangent correlation dies off. This formula, similar to Eq. (2.10), provides the exact asymptotic results. The characteristic F-R relation for large force is evidently  $f(R) = 1/(1 - R/L)^2$ , which is a distinct behavior of semiflexible elasticity [3].

In summary, the difference between the gaussian FJC and the Langevin FJC originates from the difference in conformational entropy. For the Langevin solution, one no longer assumes isotropy of the rods in the presence of a force. Rather, as the force increases,  $\vec{b}$  would be restricted to vary within a decreasing solid angle. The WLC model has the anisotropic factor built into its continuum assumption, where the tangent vectors at large extensions would be restricted to fluctuate only in certain directions. The superiority of the WLC model is that it includes rod-bending configurations which does occur in biopolymers. To end the chapter, a table of frequently used symbols and abbreviations are presented in tab.2.1.

Meaning	Symbol
end-to-end distance (extension)	$R$
end-to-end vector	$\vec{R}$
number of segments	$N$
force-extension	F-R
segment (bond) length	$b$
Kuhn length	$\ell_k$
total contour length	$L$
persistence length	$\ell_p$
angle potential constant	$K_A$
self-avoiding walk	SAW
freely-jointed chain	FJC
worm-like chain	WLC

Table 2.1: This table lists symbols and abbreviations that are frequently and consistently used throughout the report.

## Chapter 3

# Methodology: Molecular Dynamics Simulation

The F-R relation of semiflexible biopolymers is a macroscopic property which originates from the interactions between and dynamics of each monomers on a molecular scale. Molecular dynamics (MD) simulation probes such action-rich microscopic world to capture how molecular contributions build up to the macroscopic properties. MD simulation, unlike Monte Carlo (MC) simulation, presents the dynamics of molecules in physical time. It is therefore the natural approach to obtain molecular mechanical properties such as the F-R relation of biopolymers.

The simulation program used in this project is called Large-scale Atomic / Molecular Massively Parallel Simulator (LAMMPS) [12]. The software is open-source and freely downloadable. For details on the features and settings in LAMMPS, please refer to its online documentation. This chapter

has three sections. The first section discusses the simulation models; the second section covers some basic concepts of the numerical integrator; and the third section explains the method of F-R measurement.

### 3.1 The Bead-stick Model

A very common simulation model is a coarse-grained model called the bead-stick model, where several repeat units on the carbon backbone are represented by a bead. The chemical bonds that connects two monomers are represented by a stick. A schematic structure of the model is shown in Fig.

3.1. The beads are modeled by the Lennard-Jones (LJ) potential [13],

$$U^{LJ}(r) = 4\epsilon \left[ \left( \frac{\sigma}{r} \right)^{12} - \left( \frac{\sigma}{r} \right)^6 \right]. \quad (3.1)$$

The first term mimics the effect of hard sphere repulsion between the monomers. This term produces the excluded volume effect mentioned for the SAW. The second term is the induced dipole-dipole attraction between monomers. The units of the simulation are set by the  $\epsilon$  and  $\sigma$  in the LJ potential. This set of units is called the reduced LJ units. Tab. 3.1 lists the relevant units in the project. Throughout the project,  $\epsilon$  and  $\sigma$  are both set to 1. Later in the Result chapter, an estimate of the order of these units in terms of SI units



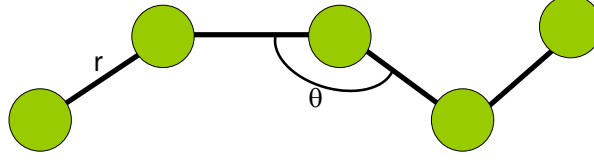


Figure 3.1: This is a schematic representation of the configuration of the bead-stick model. The circular beads represent monomers and are modeled by the LJ potential. The sticks joining the beads represent the chain of bonds between the monomers and are modeled by the FENE potential. The magnitude of  $r$  is the bond length which is determined by the combination of the LJ and FENE potentials.  $\theta$  is the angle between bonds and is used in the angle potential.

will be given.

Returning to the bead-stick model, the spring which represents the bonds between monomers is model by the finitely-extensible non-linear elastic (FENE) potential,

$$U^{FENE}(r) = \begin{cases} -\frac{1}{2} k R_0^2 \ln(1 - (r/R_0)^2) & r < R_0 \\ \infty & r \geq R_0 \end{cases}, \quad (3.2)$$

where  $k$  is the spring constant, and  $R_0$  is the cut-off spring length [13]. The logarithmic factor in the FENE potential bears no physical meaning and is strictly for computational advantage. This potential mimics the stiff and non-penetrable covalent bonds between monomers. Throughout the project,  $k$  and  $R_0$  are set to  $30 \epsilon/\sigma$  and  $1.5 \sigma$  [14]. With this value of  $k$ , the springs are stiff enough to be regarded as rigid rods in the range of forces explored. This

unit symbol	description
$\sigma$	distance
$\epsilon$	energy
m	mass
$\tau$	time = $\sqrt{m\sigma^2/\epsilon}$
T	reduced LJ temperature = $\epsilon/k_B$

Table 3.1: This table shows the set of reduced LJ units used in the simulation. The top three are the intrinsic units in a LJ potential. One can deduce all other units from these. For example, spring constants are in units of energy per *distance*<sup>2</sup> ( $\epsilon/\sigma^2$ ). Time and temperature are given in the terms of the intrinsic units in the second half of the table.

is observed and monitored by measuring the  $r$  in Fig. 3.1. The measured values of  $r$  are well within  $\pm 2\%$  of the equilibrium bond length.

The equilibrium bond length has contributions from both the LJ and the FENE potentials. A graph of the LJ and FENE potential is shown in Fig. 3.2. The LJ potential is strongly repulsive at small distance and becomes mildly attractive at larger distance. In contrast, the FENE potential is mildly attractive at small distance and highly attractive at large distance. The combination of the two potentials yields an equilibrium position where the combined potential results in a minimum at  $r=0.96\sigma$ . This is the equilibrium bond length monitored. The steepness of the slopes provides an idea of the forces required to change the bond length.

The combination of the LJ and FENE potential captures all the essential properties of a linear flexible polymer. In particular, it is very similar to the FJC model in having discrete bonds and no bending stiffness. To introduce the semiflexible case, which describes biopolymers better, a bending rigidity between the springs are introduced via the angle potential, which has the form:

$$U^{Angle}(\theta) = K_A [1 + \cos(\theta)]. \quad (3.3)$$

$K_A$  is the bending constant in units of  $\epsilon$ , and  $\theta$  is the angle between two bonds as shown in Fig. 3.1 [13]. Notice that when a bead-stick chain is

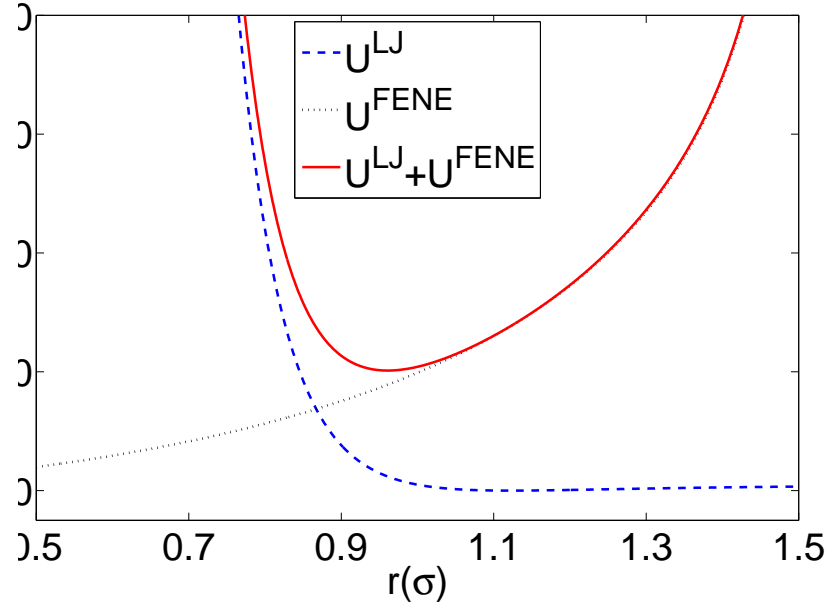


Figure 3.2: This is a plot of the LJ and FENE potentials defined by Eq. (3.1) and Eq. (3.2). For the LJ potential,  $\epsilon=\sigma=1$ . For the FENE potential,  $k=30\epsilon/\sigma^2$  and  $R_0=1.5\sigma$ . The LJ potential contributes to the repulsive interaction of the combined potential, whereas the FENE potential contributes to most of the attractive interaction. The combined potential has an equilibrium bond length of  $0.96\sigma$  [13].

straight, ie. with all  $\theta = \pi$ , the angle potential vanishes and the bending energy is minimized. Therefore, under the effect of the angle potential, a bead-stick chain tends to straighten itself to minimize the bending energy.

Quantum mechanical interactions are captured by the effective classical potentials such as the LJ, the FENE and the angle potential. The assumption made here is that the biopolymers are long chains of macromolecules which oscillate with a time scale of order of picoseconds. A coarse-grained model would be reasonable for macromolecules given that the simulation integration timestep are small enough to accurately sample molecular vibrations. The issue of the integration timestep will be discussed in the next section.

## 3.2 Numerical Integrator

In classical mechanics, a physical system is described entirely by its potentials and equations of motion (EOM). The way that MD simulations provide the mechanical properties of the biopolymers is by calculating each monomers' EOM via solving Newton's second law for an interactive many-body system numerically. The method used by LAMMPS to evaluate the

EOM is called the Verlet algorithm [13].

$$p_i(t + \frac{1}{2}\delta t) = p_i(t) + \frac{1}{2}\delta t f_i(t), \quad (3.4)$$

$$r_i(t + \delta t) = r_i(t) + \delta t p_i(t + \frac{1}{2}\delta t) / m_i, \quad (3.5)$$

$$p_i(t + \delta t) = p_i(t + \frac{1}{2}\delta t) + \frac{1}{2}\delta t f_i(t + \frac{1}{2}\delta t). \quad (3.6)$$

Notice that the momentum calculated in the first equation goes into the second equation for the evaluation of position. The position enters into the third equation implicitly since the force depends on positions. The algorithm follows the pattern alternating evaluation of momentums and positions. This algorithm is thus also called the ‘Leap Frog’ algorithm. It is a common and efficient algorithm in MD simulations.

Coming back to the issue of timestep, here  $\delta t$  is the timestep. In the project,  $\delta t$  is set to be  $0.01 \tau$  which turns out to be on the order of picoseconds. Therefore, the timestep used is small enough to properly account for the molecular vibrations.

In pulling experiments, biopolymers are placed in some solutions with a definite temperature,  $T$ . From the derivation of the F-R relation, it is clear that the entropic elasticity can only be manifested when  $T \neq 0K$ . In the simulation, the temperature is controlled by imposing a Langevin dynamics

of the form [15]:

$$\vec{f}_i - \gamma_i \vec{v}_i + \vec{R}_i(t) = m_i \vec{a}_i, \quad (3.7)$$

$$\langle \vec{R}_i(t) \rangle = 0, \quad (3.8)$$

$$\langle \vec{R}_i(t) \cdot \vec{R}_i(t') \rangle = 6k_B T \gamma_i \delta(t - t'). \quad (3.9)$$

The first equation is Newton's second law with two extra forces, namely a friction force from fluid viscosity and a colliding force from the solution particles. The second equation shows that the colliding force is random since its time average is zero. The third equation shows that the amplitude of colliding force obeys the equipartition theorem. In other words, the temperature determines the strength of collisions. These equations together mimic the kinetic random-colliding effects in a solution.

All essential dynamical effects of a biopolymer chain in solution are captured in the Langevin equations and the model potentials. In the project, we also imposed a periodic boundary condition on the system to save computing power. A flowchart of the simulation program is given in Fig. 3.3. In the process of integration, LAMMPS outputs the forces and coordinates of each monomer in every set amount of time. These measurements provide the desired F-R relation. In the project, the systems dealt with have less

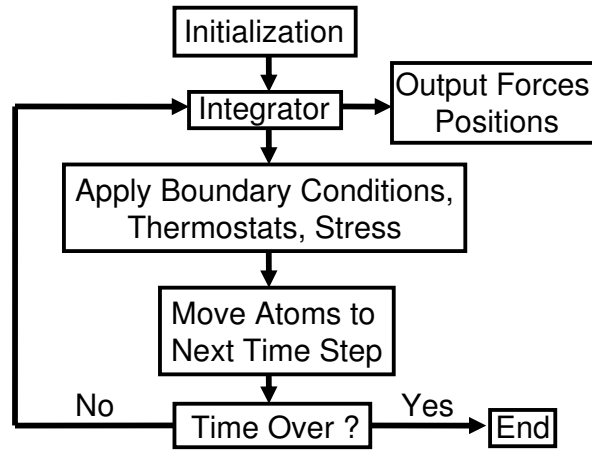


Figure 3.3: This is a schematic flowchart of the MD simulation. Initialization includes defining the potentials used and their coefficients, the starting configuration of the bead-stick chain, the dimension of the periodic boundary, the temperature, and etc. The EOM that the integrator calculates are based on the the Langevin dynamics. The integration loop calculates the EOM using the Verlet algorithm and outputs the desired dynamical quantities in every set amount of timesteps. The simulation is usually ran for 1000,000 timesteps and outputs every 1000 timesteps. [16]



than 30 monomers and a single MD simulation can usually be performed within a few minutes.

### 3.3 Force-extension Measurement

The set up of the F-R measurement is shown in Fig. 3.4. Two force sensors are arranged to be separated only in the x-direction by an amount of  $R_{sensor}$ . They are fixed at their initial position throughout the simulation. Each sensor is attached to an end of the bead-stick chain through a harmonic spring described by the harmonic potential,

$$U^{harm}(r) = K_{harm}(r - r_0)^2, \quad (3.10)$$

where  $K_{harm} = 3\epsilon/\sigma^2$  and  $r_0 = 1\sigma$ . As the bead-stick chain moves in the thermostat, it pulls on the harmonic springs, and the sensors measure the pulling forces. The value of  $K_{harm}$  is chosen so that upon a slight change of  $K_{harm}$ , the measured forces would remain the same. This ensures that the springs do not contribute to the internal structure of the bead-stick chain.

The basic idea here is that for a given  $R_{sensor}$ , there would be a mean end-to-end distance and a mean pulling force for the bead-stick chain. Therefore, by varying  $R_{sensor}$ , one obtains a set of mean force-extension data

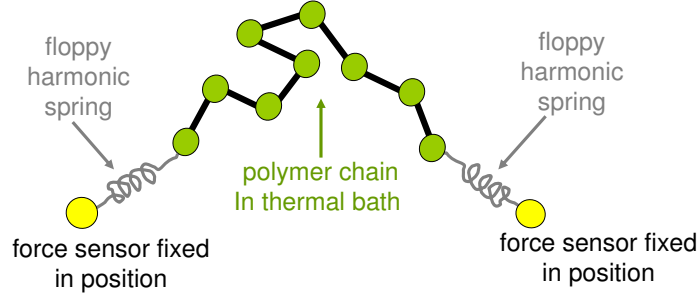


Figure 3.4: This is a schematic representation of the force measurement set up.  $K_{harm} = 3\epsilon/\sigma^2$  and  $r_0 = 1\sigma$  are used for the harmonic spring throughout the project. Remember that the whole system is placed in a thermal bath.

pairs which is the desired F-R relation. The sampling of R and the force should not be too close in time that they become correlated, otherwise the gaussian approximation would fail. The time interval used between measurements is  $1000 \delta t$  ( $10 \tau$ ).

The force sensors are just normal LJ beads. The random collision forces average to zero for these fixed sensors, so the forces measured are purely from the harmonic springs. Also, since  $R_{sensor}$  is only separated in the x-direction, the bead-stick chain only loses entropy in the x-direction. This means that one only needs to average over the x-component of the measured forces. This assumption is checked by averaging over the y, and z components of the forces. The observed average values are less than  $0.005 \epsilon/\sigma$ . Moreover, since there is no physical difference between the left and right

sensors, a mean force is computed for each sensor. The final mean force is the average of the amplitude of the two mean forces.

## Chapter 4

# Results

In this chapter, the results from the simulation are shown and compared to the theory. The accuracy and quality of the simulated result is extremely nice. In the first section, general properties of the random walks are tested as a basis of later works. In the second section, the small extensions region is examined. In the third section, the F-R relations for different flexibility are shown and fitted with the FLC and WLC solutions. Surprisingly, there appeared an elastic region where the WLC cannot describe. That is a transition from semiflexible to rigid-rod-like. In the last section, issues on time scale of the force convergence are investigated.

The validity of MD simulation to reproduce experimental results is one of the focuses in this chapter. Since the theory of F-R relation is well established, a good match with the theory should be an indication of validity. This will become a stepping stone to investigate the more complicated case of biopolymer networks. Another focus in this chapter is to explain the physics behind the biopolymers with the aid of the simulation data.

Throughout the project, except when testing the R-N relation of the self-avoiding walk, the LJ energy parameter  $\epsilon$  is set to be 0. In this way, the bead-stick model becomes a jointed-stick model which is really similar to the FJC model. All the non-specific interactions are also set to zero to ensure ideal random walk.

## 4.1 Properties of Random-Walking Chain

In this section, the results for the R-N relation and the distribution of R are shown. These results are the first checks of the validity of using MD simulation to reproduce experimental force-extension data. The goal is to see the trend discussed in the Properties of Polymer Chain section rather than matching up the details.

The simulation set up is simply letting the bead-stick chain move freely in a thermostat. By varying the number of segments N and calculating the corresponding mean end-to-end distance R, one obtains the R-N relation. The result is shown in Fig. 4.1. For the ideal random-walk data set labeled with  $\epsilon = 0$ , Eq. (2.2) fits very nicely. For the SAW data set labeled  $\epsilon = 1$ , the effect of volume exclusion comes in and the corresponding theory from Eq. (2.3) requires an exponent of 1.2. From Fig. 4.1, one sees that Eq. (2.3) fits the data reasonably well. The remark here is that the trend of exponent

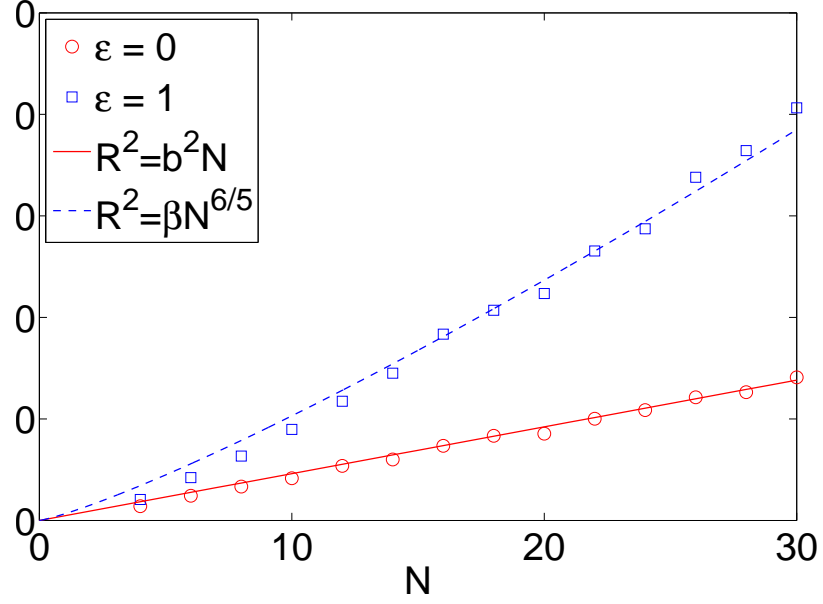


Figure 4.1: This is a plot of the R-N relation N for both the random and self-avoiding walk. The simulation runs with  $T=1$ . The data labeled with  $\epsilon = 0$  is the ideal random walk, while the  $\epsilon = 1$  data is the self-avoiding walk. For the random walk, the value of  $b$  is 0.96, the bond length. Using that value, the data matches the theory. The fitted value of  $\beta$  in the SAW is 1.3. This fit is not as promising, but still catches the trend of the exponent.

increase from the ideal random walk to the SAW is captured quite well.

For the second test, on the distribution of  $R$ , a histogram of all the measured  $R$  for the  $N=10$  case is plotted. The result is shown in Fig. 4.2. The distribution should correspond to note that Eq. (2.5) is the normalized probability distribution, whereas the histogram is not. Therefore, a scaling factor is multiplied to  $P(R)$  so that the data is comparable to theory. The histogram nicely captures the shape of the distribution curve. One may also

look for the most probable  $R$  using Eq. (2.5). By setting the derivative of the equation to 0 and solving for  $R$ , one obtains

$$R_{peak} = \sqrt{\frac{2N}{3}} b, \quad (4.1)$$

which using  $N=10$  and  $b=0.96$  yields  $R_{peak}=2.48\sigma$ . The peak in the graph is about  $R=2.5\sigma$ , which again follows the right trend. To conclude this section, the two results establish the first foundation of the validity of using MD simulation to model at least the flexible polymers.

## 4.2 The Entropic Spring Constant

Knowing that the simulated distribution of  $R$  matches the theoretical distribution, we now move to the  $F$ - $R$  relation of the flexible case. As shown in Eq. (2.8), the polymer chain at low extension acts like a Hookeian spring with  $T$  and  $N$  dependence. In this section, the low extension region of the simulated  $F$ - $R$  relations are compared with the linear elasticity.

The simulation set up for obtaining the force-extension relation is outlined in the Measuring Force-extension section. A sample result for the  $N=16$ ,  $T=0.5$  case is shown in Fig. 4.3 with the gaussian FJC theory. One can see that the data describes the theory reasonably well up to an extension of about half the total contour length  $L$ . After that, the data diverges

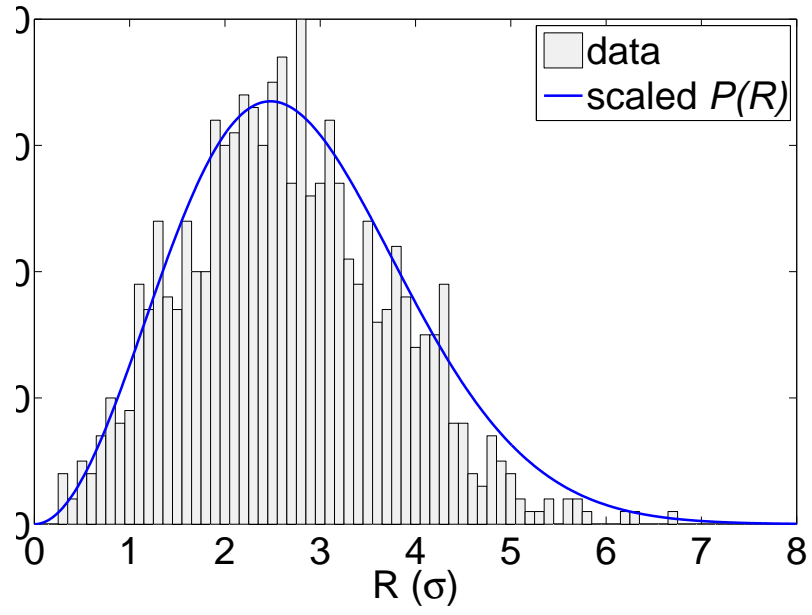


Figure 4.2: The histogram is the simulated distribution of  $R$  for the  $N=10$ ,  $T=1$  case. The mean of the distribution is  $2.66\sigma$ . The solid line is a scaled distribution of  $R$  given by Eq. 2.5. For comparison purposes, a scaling factor of 100 is chosen. Note that scaling does not change the relative shape of the distribution. All entropic information is unaltered.



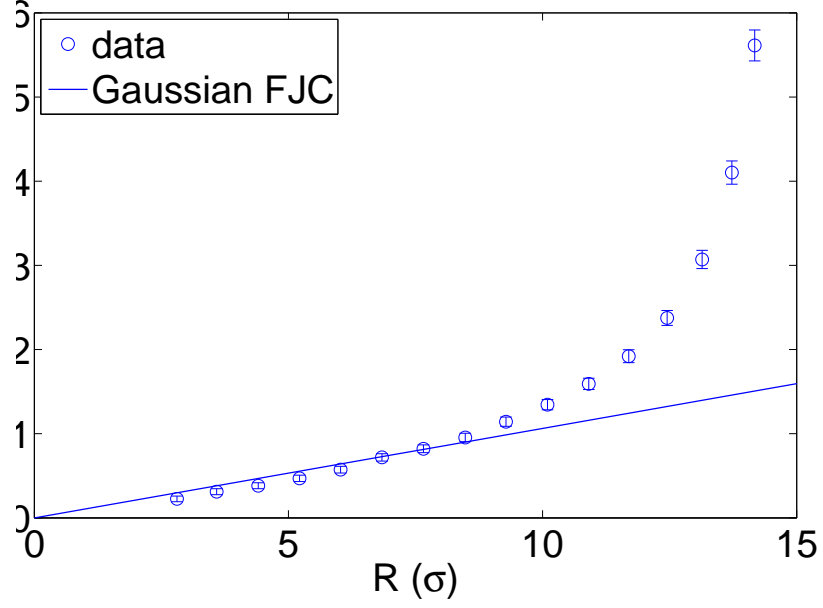


Figure 4.3: This is a plot of a sample force-extension data of the flexible chain for the  $N=16$ ,  $T=0.5$  case. The solid line shows the prediction from the gaussian FJC for small extensions. The errorbars shown are on the most part the same size as the markers, so errorbars will be omitted for all later results. The parameter used in the gaussian FJC approximation are  $b=0.96\sigma$ ,  $N=16$ ,  $k_B=1$ , and  $T=0.5$ .

significantly from the theoretical line. The uprise for large extensions will be discussed later.

To check the dependence given in Eq. (2.9), two sets of force-extension curves are obtained. One set has a fixed value of  $N$  with different temperature to test the  $T$  dependence of the  $k_{entropy}$ , while the other set has a fixed value of  $T$  with varying  $N$  to test the  $N$  dependence. A sample result is shown in Fig. 4.4. As seen in Fig. 4.3,  $k_{entropy}$  is just the slope of the linear

region at small extensions. Through linear fittings to all the force-extension curves in the linear region, two sets of simulated  $k_{entropy}$ , one a function of T, the other of N, are obtained. From Fig. 4.4, the general right trend of dependence on T and N is observed. The right hand graph with the T dependence clearly shows that as T increases, the slope of the F-R curves with all other factors fixed also increase. In the same token, the graph on the left shows that as N increases, the slope of the force-extension decreases. One remark on top of the physics here is the power of simulation. It is often difficult to eliminate undesired variables in a real experiment, but it is very easily done in simulation with arbitrary precision.

A more quantitative analysis is done by plotting the fitted values of  $k_{entropy}$  against their variables. The result for the temperature dependence is shown in Fig. 4.5, and the result for the N dependence is shown in Fig. 4.6. Following the above prescribed method, one obtains from the slope of the left graph of Fig. 4.4 the bottom square data points in Fig. 4.5. As the graph shows,  $k_{entropy}$  is perfectly linearly proportion to T for the N=32 case. The other three lines of data points above are for chains with different values of N as shown in the legend. The linear T dependence of  $k_{entropy}$  enters into all four chains nicely. One thing to note is the small discrepancy for the chains with small N. This is a warning that for N smaller than 8, the

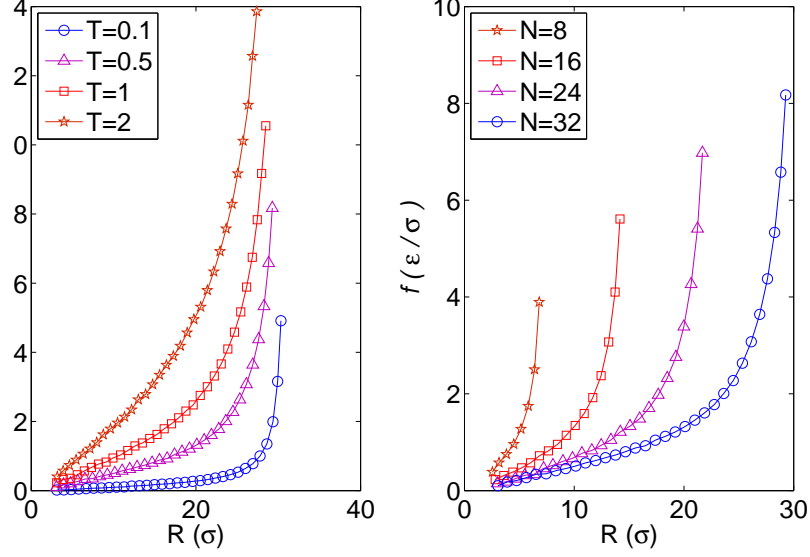


Figure 4.4: The left hand side plot is a set force-extension relations with the fixed  $N=32$  and varying  $T$ . The right hand graph is another set with fixed  $T=0.5$  and varying  $N$ . The linear slopes on the graph at low extension are the  $k_{entropy}$  for that curve. On the left plot, the slope increases as  $T$  increases. For the right hand plot, as  $N$  increases, the slope of decreases. This is qualitatively right.

theoretical prediction of the rubber elasticity starts to break down, which is reasonable in view of the assumption that  $N \gg 1$ .

For the  $N$  dependence, the right hand graph in Fig. 4.4 corresponds to the cross data points in Fig. 4.6. Here, one sees that  $k_{entropy}$  is more or less linearly proportional to  $1/N$  for small value of  $T$ . As the temperature gets higher, the inverse  $N$  dependence is lost. The difference is quite significant at  $T=2$ . Also, the deviation from a pure  $1/N$  dependence is caused by the

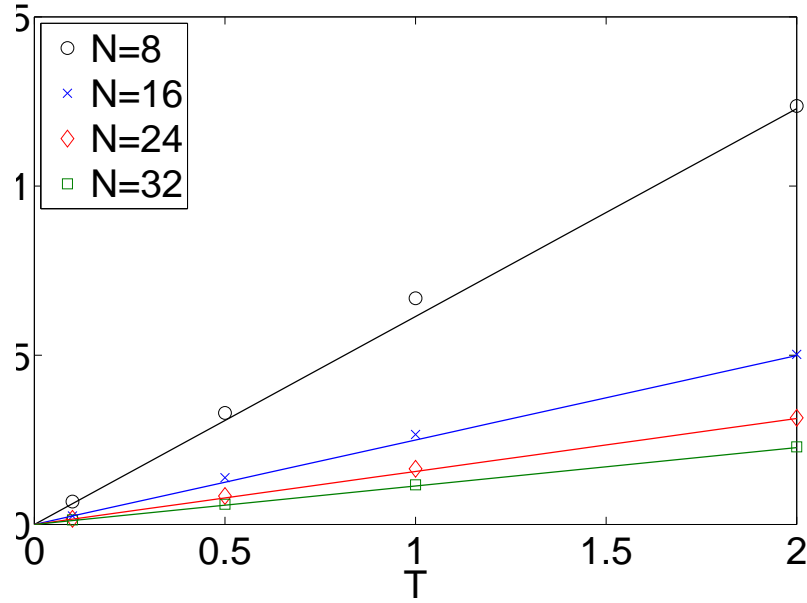


Figure 4.5: This is a plot of the temperature dependence of  $k_{entropy}$  for 4 chains, each with a different number of  $N$ . This corresponds to four of the right hand graphs in Fig. 4.4. The lines are best linear fits to the data points. The fitting model is  $\alpha T$ , where  $\alpha$  is the fitting parameter. The value of  $\alpha$  is not of concern here. The thing to note is the linear dependence of  $k_{entropy}$  on  $T$ .

data points with the highest  $1/N$  values, which corresponds to the lowest  $N$ . This again points to the unreliability of simulation with  $N$  smaller than 8. Quantitatively, this result shows that the upper limit on  $T$  should be about 0.5 and the lower limit on  $N$  should be about 17. These values then are used for all of the following results unless otherwise indicated.

Another factor that comes into the  $N$  dependence is in the exact FJC

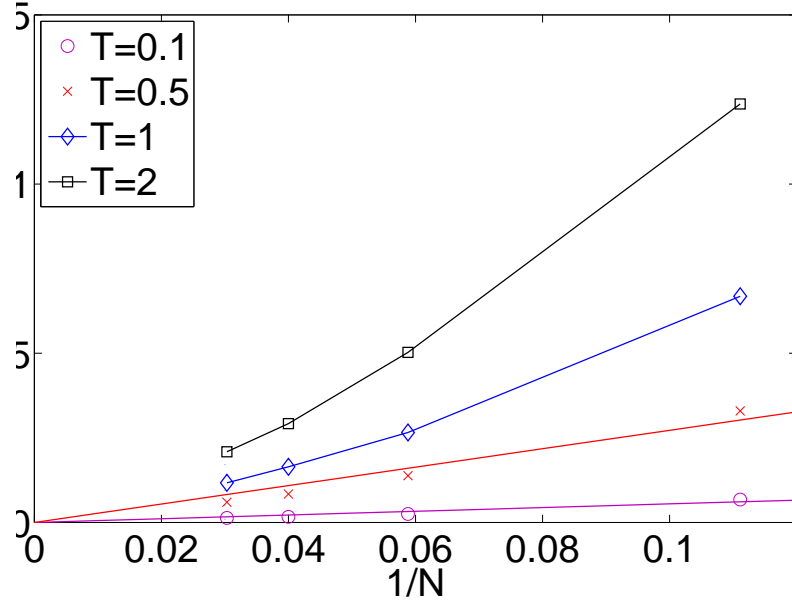


Figure 4.6: This is a plot of the  $N$  dependence of the entropic spring constant. The two lines through the bottom two sets of points are linear fits of form  $\alpha/N$ . The top two sets are not fitted since it is obvious that they are not linear. Here we learn that the  $N$  dependence of  $k_{entropy}$  is not simple.

solution. In the approximation of Eq. (2.11), one sees that the force does not simply depend on  $1/N$  but includes a correction factor that also depends on  $N$ . This is basically why the low  $N$  limit does not work. The correction terms become dominant even at small extensions. This is actually apparent in the right hand graph in Fig. 4.4. The  $N=8$  curve has basically no linear region, whereas the  $N=32$  chain has a much longer linear region. When very large  $N$  is considered, what one gets is a rubber whose  $R_{peak}$  is much smaller

than the characteristic linear range. With this kind of chain, it seems like it is forever flexible.

### 4.3 Elasticity Spectrum

In this section, the effect of the angle potential comes into play to turn the flexible chain into a semiflexible chain. The amazing phenomenon is that as the angle potential is increasing, a spectrum of elasticity occurs with definite distinguishable feature on the force-extension graphs. The spectrum consists of the flexible region, the semi-flexible region, and the rigid-rod-like region.

To start, we consider the form of the Langevin FJC solution. In Eq. (2.10), the extension is normalized by the total contour length  $L$ . In doing that, the  $N$  dependence of the force-extension relation disappears. This means that given the same temperature, chains with reasonable number of segments, ie. greater than 8, should collapse onto one curve. The result for this is shown in Fig. 4.7 where all the force-extension curves collapsed beautifully upon normalization.

This is actually a surprising common feature in all of Eq. (2.8), Eq. (2.10), and Eq. (2.13) that upon rescaling with the  $L$ , the F-R relations do not depend on  $N$ . This is a bit counter-intuitive since chains with more segments surely have access to more configurations than chains that have

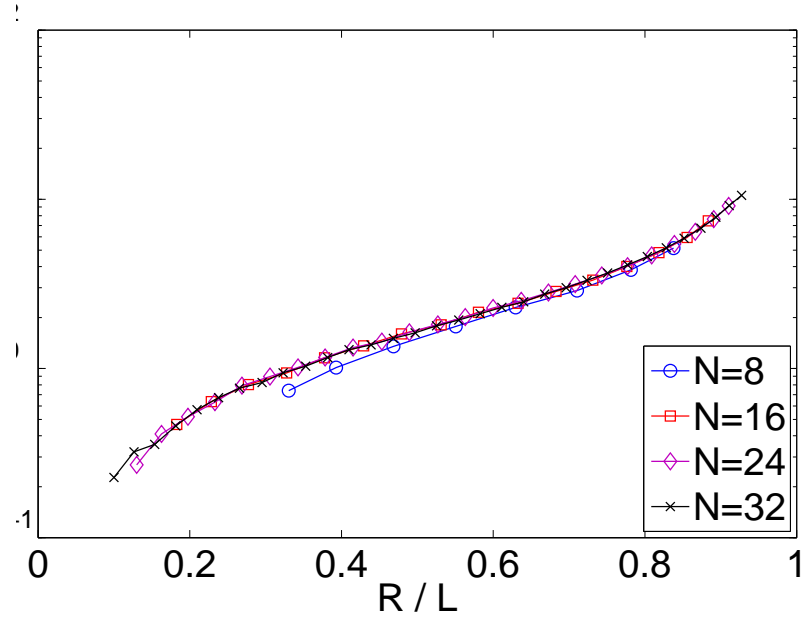


Figure 4.7: This is a plot of the normalization of the F-R relations for chains in  $T=0.5$  Langevin thermostat. The curves with different  $N$  are normalized by their corresponding total contour lengths  $L=Nb$ . Note that the y-axis is in log scale. Without normalization, this graph is the same as the one on the right in Fig. 4.4. With normalization, the  $N$  dependence disappears and the curves collapse into one beautifully as the F-R formulas suggest.

less. The trade-off may be a balance in the position and the momentum space. A long chain, though occupies more states in position space, cannot move as fast as a short chain that has the same energy, and thus, occupies less states in momentum space. In any case, the conclusion is that  $N$  is not a parameter which alters the force-extension relation when the entire extension region is in perspective.

Fig. 4.7, with the  $\log(f)$  scale, is the format that is more popular in journal articles. Matching the simulation result with experimental data in the articles [17], one finds that the simulation force unit is on the order of 0.1 piconewton.

### 4.3.1 From Flexible to Semiflexible

The same sample force-extension curve from the Entropic Spring Constant section is compared to the Langevin FJC solution here. The result is shown in Fig. 4.8. In Fig. 4.8, the Langevin FJC solution fits the curve perfectly, capturing all the details of the force uprise. The remarkable agreement between the simulation and the theory again suggests the power of MD simulation to bridge theories to experiments.

To explain more of the physics of the force uprise for the flexible case, we first consider the linear elasticity. In that region, each segment actually



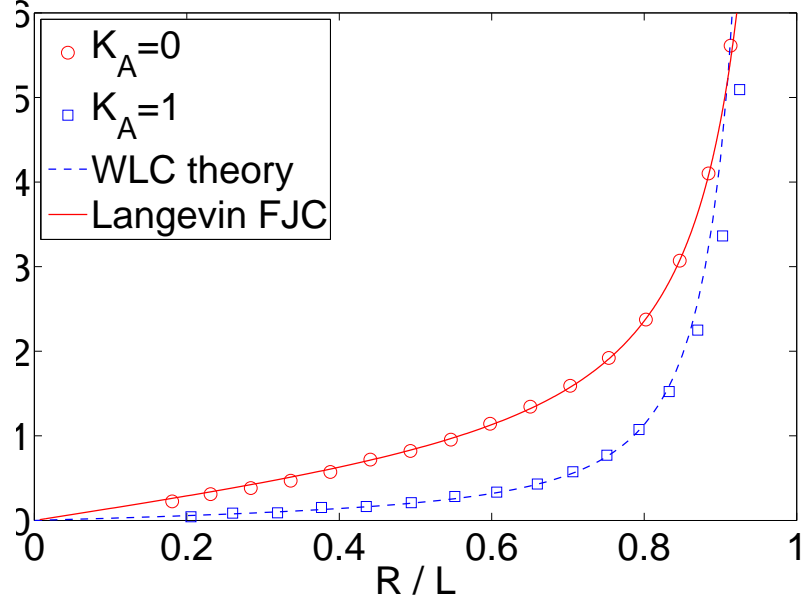


Figure 4.8: This is a plot of the force-extension for the flexible and semiflexible cases with the theoretical models. To fit the flexible data labeled  $K_A=0$ , the Langevin FJC solution is used. The fitting parameter is  $\ell_k$ , which should be  $b/2=0.48\sigma$  for ideal chains. The fitted value of  $\ell_k$  turns out to be  $0.53\sigma$ . The two values are quite close. For the semiflexible data labeled  $K_A=1$ , the WLC interpolation solution is used. The fitted parameter gives  $\ell_p=3$ .

behaves as if it does not feel the force since isotropic assumption of the gaussian approximation still works. However, at large extensions, the chain runs out of length and each segment is eventually forced to line up. In this region, the transverse vibration of the chain becomes important and dominant. From an energy point of view, the excitation of the transverse modes is the cause of the uprise.

On the same graph, there is also the first semiflexible F-R with the angle potential constant  $K_A = 1$ . Comparing the semiflexible data to the flexible case of  $K_A = 0$ , the force uprise of the semiflexible case at large extensions is shaper, more sudden. This is an indication of transition to the semiflexible case. Physically, semiflexible chains have more of the transverse excite modes and less of the other conformations due to the bending rigidity. This explains why it requires less force to pull on a semiflexible chain at small extensions and why the force required grows sharply. Moreover, notice that the interpolation formula fits quite well for most of the parts, but at very large extensions, the analytical curve rises before the simulation data does. The discrepancy may have many reasons. The obvious one is that the fitted model is just an interpolation formula. The exact numerical solution may fix the discrepancy easily. A more interesting but also valid reason is that the WLC model can only cover a range of semiflexibility and thus, cannot capture all of the semiflexible spectrum. This is intuitive when one considers a case like  $K_A=0.5$ , where the rise of the force-extension curve would be expected to lie in between the exact FJC solution and the WLC solution. This is a motivation for development of even more realistic models such as the extensible-FJC and extensible-WLC model.

One interesting fact that has been neglected until now is that at large

extensions, the power law F-R relation for the WLC is different from that of the Langevin FJC. From Eq. 2.13 and Eq. 3.9, one can deduce the power laws. For the WLC, the force rises like  $1/\varepsilon^2$ , whereas the Langevin chain rises like  $1/\varepsilon$ . The  $\varepsilon$  here is a number approaching zero. Recently, Shaqfeh et al. have demonstrated that the entropic force singularity is related to inertialess elastic recoils [18]. Borrowing the idea of elastic recoil, one can argue that a WLC at large extensions recoils harder than a FJC. Therefore the difference between the two models are not only in the bending energy, but also in their response to outside tension. This may be an explanation for the difference in the force uprise.

### 4.3.2 Angle Potential and Persistence Length

Here, chains with increasing values of  $K_A$  are implemented. The results for the  $K_A$  equals 2 and 3 are plotted in Fig. 4.9. In the graph, a very nice agreement between the WLC theory and simulation data is again manifested. Notice that unlike what happened in the  $K_A = 1$  case, the analytical curve captures the rise of the force very well for  $K_A$  equals 2 and 3. However, if one looks closely, especially for the  $K_A=3$  case, one sees discrepancy between the theory and the data points just before the force rises. This is yet another transition in the elasticity spectrum to the buckling region which will become

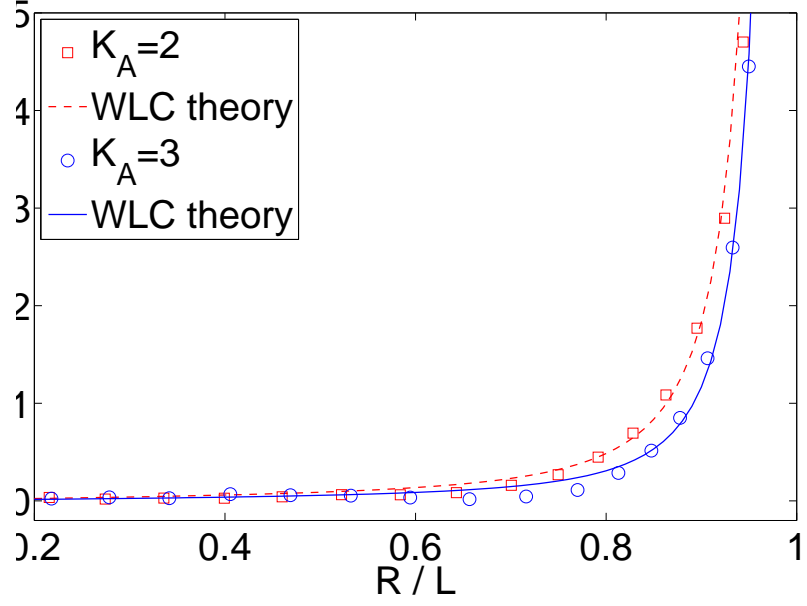


Figure 4.9: This is a plot of the F-R relation for  $K_A$  equals 2 and 3. The WLC solution describes these two cases almost perfectly. The fitted persistence lengths are given in Tab. 4.1.

apparent in the next section with higher values of  $K_A$ .

Before turning to the new transition, the fitting parameter in the WLC interpolation formula is worth mentioning. In fact, the fitting parameter, persistence length  $\ell_p$ , is an important feature of the semiflexible chain. The result of several fits are given in Tab. 4.1. It is mentioned in the Theory chapter that  $\ell_p$  is the characteristic length over which the neighboring tangent vectors become uncorrelated. The persistence length takes into account all kinds of bending rigidity including fixed angle and limited bending

---

Temp	$K_A$	$\ell_p$
0.5	1	3
0.5	2	7
0.5	3	11
1	3	4.8
1	4	11

Table 4.1: This is a table of fitted  $\ell_p$  from the WLC model for different  $K_A$ s. For the T=1, at  $K_A=4$ , the simulation data reaches the transition  $K_A$  value to the semi-rigid rod region. For the T=0.5 case, the transition occurs at  $K_A=3$ .

between bonds. The stronger the bending rigidity becomes, the longer the persistence length becomes because the tangent vectors are restricted more and more and thus become more correlated. This is evident from the table. Also, from the table, one sees that for the same  $K_A$ , chains at higher temperature has a shorter  $\ell_p$ . This is reasonable since the chain having more energy in higher temperature, can overcome more bending rigidity.

### 4.3.3 Transition to Semi-rigid Rod

As  $K_A$  increases to 3, the WLC formula no longer applies because the chain has entered into a region where it buckles. In Fig. 4.10, force-extension curves with higher  $K_A$  values are plotted. There are a few interesting features in this graph that are distinctly different from those of the flexible and semi-flexible cases. First, comparing the first data point at the shortest extension of every curve, one sees that as the  $K_A$  value increases, the required

”pulling” force increases. Second, when  $K_A$  equals to 10 and 20, the forces decrease mildly until quite a large extension. When  $K_A$  equals to 3 and 4 in the same region, the curves seem to rise a bit then decrease. Third, there is a pronounced decrease in force before the turning up point. The slopes at this region is more negative for larger  $K_A$ . Fourth, curves with higher  $K_A$  turn at larger extension and more sharply. Finally, curves with higher  $K_A$  values generally require higher stretching force for the entire extension region.

To explain what is happening, imagine a slightly compressible rigid rod with a length of 0.9 unit. As one tries to change  $R$  to 0.1, a large pushing force is required. The rigid rod is said to buckle in this region of extension. As the extension approaches its original length, the required pushing force suddenly decreases and would reach the lowest value. This is an extreme illustration that shows why the force decreases as one ”pulls” on the chain. The reason is that at a high value of  $K_A$ , one is actually pushing to deform the chain instead of pulling. For the final uprise of the force-extension, the physics should be the same as a semiflexible chain since the WLC formula captures the rise of the  $K_A=3$  curve, which can be considered as inside the new region already. Physically speaking, the new phenomenon occurs because the pushing force emerges. However, at large extensions, the old

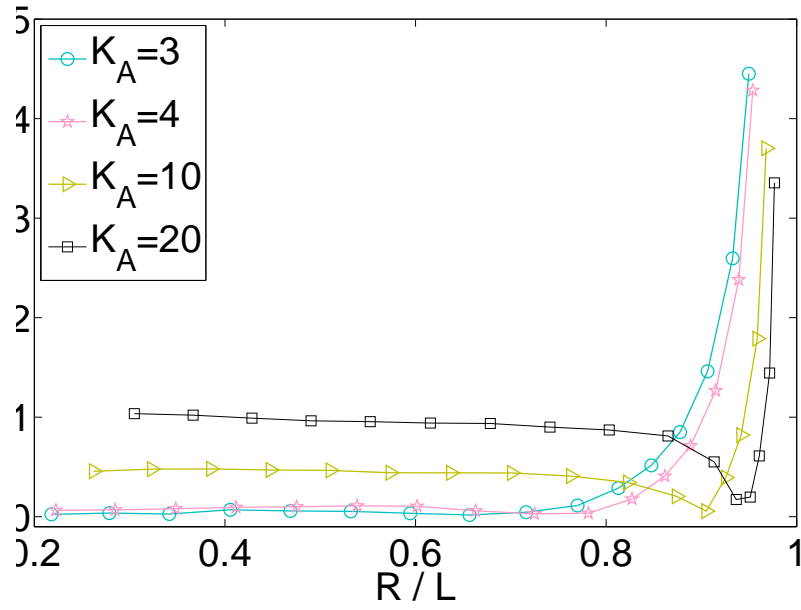


Figure 4.10: This is a plot of the force-extension of high values of  $K_A$ . High values mean that the simulation model in this region of  $K_A$  is no longer well described by the WLC model. In this new region of elasticity spectrum, the chains are more rigid-rod like, and experience both pushing and pulling forces. The result is the previously unseen negative slopes and equilibrium lengths.

pulling force does not change; therefore, the F-R behavior at large extensions should still maintain semiflexible. The transition curves to this region contains a small hill before the force rises. This transition can be called a semirigid-rod transition.

## 4.4 Force Convergence

In reality, there are considerably more naturally cross-linked semi-flexible biopolymers than single-chain biopolymers. In determining their mechanical properties, one performs the usual pulling experiment. The measured force of course is intrinsically a statistical object which requires certain number of sampling for the measurements to be reliable. This is controlled by the pulling velocity in experiments. Pulling experiment on cross-linked network might often be time-consuming; therefore, it is good to have a rough idea of the highest pulling velocity given that the F-R curve is reliable and stabilized. In this section, MD simulation explores the force-extension curve under non-zero pulling velocities.

Previous set up for F-R measurements correspond to a velocity of zero. To introduce a velocity, one simply allows one of the force sensors to move instead of having them both fixed. The data points for pulling are obtained through averaging the force-extension events with respect to time. The total



time needed for the the chain to be pulled straight, which is the total time in a simulation, is equally divided into 15 slots. Each slot will give a time averaged force-extension data point. The obtained results are plotted in Fig. 4.11.

As expected, for large velocities, the averaged force-extension data are all over the place. Not enough configurations are sampled to give a reliable average. The lower velocity cases of course then give a time averaged F-R that resembles more of the stable force-extension curve. However, this is not precise enough to compare to the theory. Therefore, an upper bound on the velocity in the simulation would be around  $0.0001 \sigma/\tau$ . In real experiments, the pulling velocity is on the scale of  $\mu m/s$ . Given more time, one may produce some useful results to aid experiments.

Emerging from the previous discussion about force converging to a reliable average, one can check the force convergence with respect to time for the stationary case. The result is plotted in Fig. 4.12 for chains with different bending rigidity. Surprisingly, even though the magnitude of fluctuation is different for chains with different  $K_A$  values, the time scale on which the force converges does not change in the presence of bending rigidity. This means that the obtaining of a reliable force-extension relation for any linear semiflexible biopolymer does not require a more delicate pulling velocity.

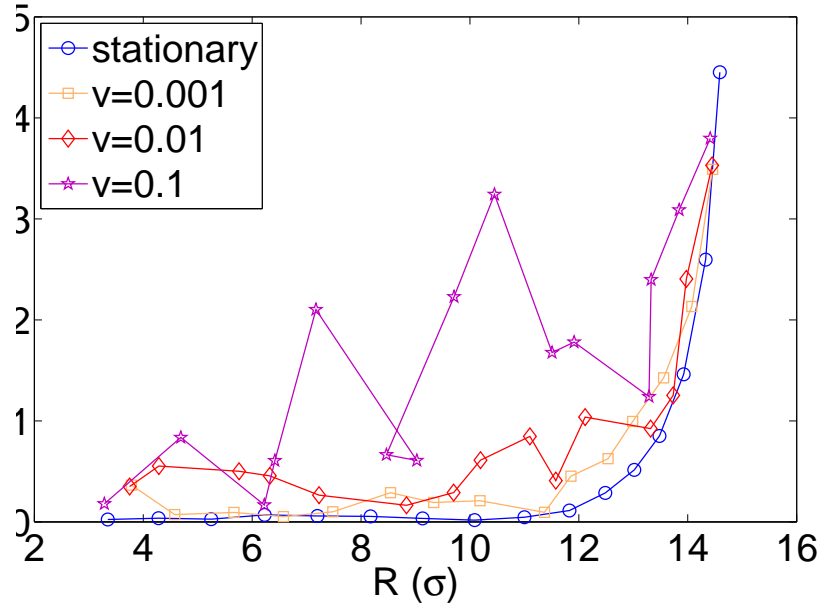


Figure 4.11: This is a F-R relation plot under pulling tension. The tension comes from the constantly moving harmonic spring and force sensor. The chain being pulled has  $K_A=3$ . The corresponding  $\ell_p$  of this chain is more comparable to a cross-linked network's characteristic  $\ell_p$ . Expectation of unreliable F-R average is confirmed. As the velocity decreases, the F-R converges better and is thus more reliable.

One can just pull as fast as if they were fully flexible polymers.

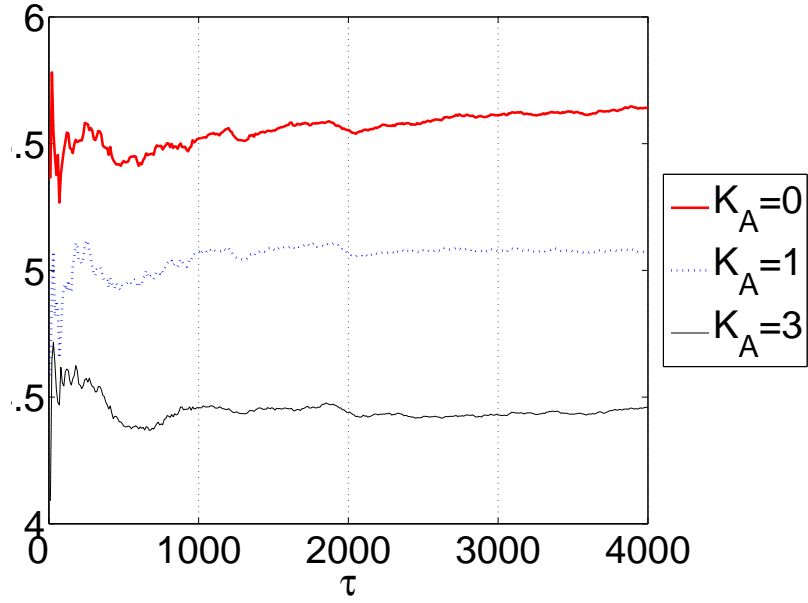


Figure 4.12: This is a plot of the time scale of force convergence. The three plots represent the flexible and semiflexible chains with an initial separation of  $R_{sensor}=16\sigma$ . The x-axis is time. The y-axis is the time averaged force up to the index  $\tau$ . The graph basically shows the timescale of averaged force convergence. Regardless of the flexibility, the forces converge at about  $\tau=2000$ .

## Chapter 5

# Conclusion

In the project, we used MD simulation to implement a coarse-grained jointed-stick chain (JSC) with varying bending rigidity. The JSC is placed in a solution with finite temperature through imposing Langevin dynamics on the system. The measured F-R relations for different value of bending angle constant  $K_A$  fall into three categories in an elastic spectrum, each has a distinct behavior.

In the first region, no bending rigidity is imposed on the JSC and the JSC becomes a resemblance of the FJC. The gaussian approximation of the FJC predicts a chain scaling governed by Eq. 2.2 and the distribution of  $R$  given in Eq. 2.5. The scaling of the JSC and its probability distribution follows the trend of the equations nicely. This means that the JSC obeys gaussian statistics and is isotropic. Given that  $T \propto 0.5$  and  $N \propto 17$ , the JSC also shows the right dependence on  $T$  and  $N$  as the Hookeian entropic spring constant suggests for  $R \propto 0.5L$ . However, at  $R \propto 0.5$ , serious deviation from the gaussian FJC model is observed. This is corrected when one use Langevin

FJC statistics to account for the finite extensibility of a chain. With the corrected conformational entropy, the F-R obtained from the JSC captures all the details of the Langevin FJC solution of F-R relation. The distinct F-R behavior in this region is a  $1/\varepsilon$  uprise in force at larger extension, where  $\varepsilon \rightarrow 0$ .

The JSC model is made semiflexible by introducing a non-zero bending rigidity, whereas the analytical model is made semiflexible by the introduction of a continuum model, the WLC. The WLC is different from the FJC in that its energy depends on the curvature of the configuration. The curvature in a stretched WLC corresponds to the forbidden rod-bending in a FJC. The resulting difference in F-R relation is at large extensions, where the force rises like  $1/\varepsilon^2$  for the WLC and  $1/\varepsilon$  for the FJC. Fortunately, the semiflexible JSC again captures all the details of the WLC solution up to large extensions. This shows that the angle potential energy in the JSC recompensed for the rod-bending energy in the WLC. The distinct F-R behavior in this region is the  $1/\varepsilon^2$  force uprise at large extensions.

In the last region, a transition from semi-flexible to semi-rigid rod is observed. The distinct behavior for F-R curves in transition is a small hill before the force ascends. In this region, a pushing force emerges from high bending rigidity and causes a non-monotonic F-R relation. In the pushing

region, F-R slopes are negative, whereas in the pulling region, the F-R slopes are positive. At the turning point, the JSC is in its equilibrium R. This region in the elasticity spectrum goes beyond the description of the WLC.

Toward the end, the reliability of the F-R relation under tension is briefly explored. The resulting constraint on the highest pulling velocity is  $0.0001 \tau$ . Finally, the stability of force convergence for different flexibilities is tested. The surprising result is that regardless of bending rigidity, the forces converge at the same rate. This implies that as far as pulling experiments are concerned, the upper bound for velocity applies in all of the flexible and semiflexible region.

## 5.1 Outlook

The flexible and semiflexible simulations are established well upon the theories. As presented in the report, most of the results obtained match the theoretical prediction quite well. This firm foundation laid is a stepping stone to extend the simulation to the cross-linked semiflexible network. To that end, almost all the simulation set up remains the same except a new starting configuration of randomly cross-linked semiflexible chains. Other things one can try are to match the simulation models with new modified models with more parameters such as the extensible-WLC model. Applying

stress and strain can also be interesting. The diversity of polymer physics one can explore from this point onward is great.

# Bibliography

- [1] Smith, S. B., Finizi, L., Bustamante, C., *Science* **1992**, 258, 1122.
- [2] Bustamante, C., Bryant, Z., Smith, S. B., *Nature* 421, 23 Jan. **2003**.
- [3] Marko, J.F. Siggia, E.D., *Macromolecule* **1995**, 28, 8759-8770.
- [4] Gardel, M.L. et al., *Elastic Behavior of Cross-linked and Bundled Actin Networks*, *SCIENCE* **2004**, Vol. 304, 1301-1305.
- [5] Hess, H., Bachand, G. D., Vogel, V., *Chemistry - A European Journal* 10, **2004**, 2110-2116.
- [6] Paul J. Flory, *Principles of polymer chemistry*; Ithaca, NY : Cornell University Press, **1953**.
- [7] Barrat, J.L., Hansen, J.P., *Basic Concepts for Simple and Complex Liquids*; NY : Cambridge University Press, **2003**, Section 1.5.
- [8] Boal, David H., *Mechanics of the cell*; NY : Cambridge University Press, **2002**.



- [9] Kuhn, W., Grun, F., *Kolloid-Z.* 101, **1942**, 248V271.
- [10] Cohen, A., *Rheol. Acta* 30(3), **1991**, 270-273.
- [11] Landau, L. D., Lifshitz, E. M., *Theory of Elasticity*, NY : Pergamon Press, **1970**. 17-82.
- [12] LAMMPS official website.  
<<http://www.cs.sandia.gov/~sjplimp/lammps.html>>.
- [13] Allen, M.P., *Introduction to Molecular Dynamics Simulation*, published in *NIC Series* **2004**, Vol. 23, 1-8.
- [14] Kroger, M., Loose, M., Hess, S., *J. Rheol.* 37, **1993**, 1057-1080.
- [15] Steinbach, P.J., *Introduction to Macromolecular Simulation*, **2005** Aug. 12. <[http://cmm.info.nih.gov/intro\\_simulation/](http://cmm.info.nih.gov/intro_simulation/)>. Accessed 2005 Nov.
- [16] J. Kolhe, *Parallelization of Carbon Nanotube Based Composites* (MA thesis, The Florida State University, **2004**), 9-13.  
<<http://etd.lib.fsu.edu/theses/available/etd-07122004-165317/>>.  
Accessed 2005 Nov.
- [17] Zhou, H., Zhang, Y., Yang, Z. O., *Phys. Rev. E.* 62(1), **2000**, 1045-1057.

- [18] Shaqfeh, E. S. G., McKinleyb, G. H., Wooc, N., Nguyend, D. A., Sridhar, T., *J. Rheol.* 48(1), **2004**, 209-221.